

The evolution and distribution of recycled oceanic crust in the Earth's mantle: Insight from geodynamic models

Jun Yan^a, Maxim D. Ballmer^{b, a, c}, and Paul J. Tackley^a

^a Institute of Geophysics, ETH Zurich, Zurich, Switzerland

^b Department of Earth Sciences, University College London, London, United Kingdom

^c Earth-Life Science Institute, Tokyo Institute of Technology, Tokyo, Japan

Corresponding author: Jun Yan (jun.yan@erdw.ethz.ch)

Highlights:

- Compositional mantle layering is robustly predicted despite whole-mantle convection.
- Basalt-enhanced reservoir forms in the MTZ, independent of mantle viscosity profile.
- Basalt fraction in the MTZ is laterally variable, ranging from ~30% to 50%.
- A layer beneath the MTZ displays significant (40%~80%) enrichment in harzburgite.
- The bulk-silicate Earth may be enriched in basalt relative to upper-mantle pyrolite.

Keywords: recycled oceanic crust, compositional mantle layering, chemical heterogeneity, mantle transition zone, thermochemical convection

Abstract

A better understanding of the Earth's compositional structure is needed to place the geochemical record of surface rocks into the context of Earth accretion and evolution. Cosmochemical constraints imply that lower-mantle rocks may be enriched in silica relative to upper-mantle pyrolite, whereas geophysical observations support whole-mantle convection and mixing. To resolve this discrepancy, it has been suggested that subducted mid-ocean ridge basalt (MORB) segregates from subducted harzburgite to accumulate in the mantle transition zone (MTZ) and/or the lower mantle. However, the key parameters that control basalt segregation and accumulation remain poorly constrained. Here, we use global-scale 2D thermochemical convection models to investigate the influence of mantle-viscosity profile, planetary-tectonic style and bulk composition on the evolution and distribution of mantle heterogeneity. Our models robustly predict that, for all cases with Earth-like tectonics, a basalt-enriched reservoir is formed in the MTZ, and a harzburgite-enriched reservoir is sustained at 660~800 km depth, despite ongoing whole-mantle circulation. The enhancement of basalt and harzburgite in and beneath the MTZ, respectively, are laterally variable, ranging from ~30% to 50% basalt fraction, and from ~40% to 80% harzburgite enrichment relative to pyrolite. Models also predict an accumulation of basalt near the core mantle boundary (CMB) as thermochemical piles, as well as moderate enhancement of most of the lower mantle by basalt. While the accumulation of basalt in the

MTZ does not strongly depend on the mantle-viscosity profile (explained by a balance between basalt delivery by plumes and removal by slabs at the given MTZ capacity), that of the lowermost mantle does: lower-mantle viscosity directly controls the efficiency of basalt segregation (and entrainment) near the CMB; upper-mantle viscosity has an indirect effect through controlling slab thickness. Finally, the composition of the bulk-silicate Earth may be shifted relative to that of upper-mantle pyrolite, if indeed significant reservoirs of basalt exist in the MTZ and lower mantle.

1. Introduction

Mantle convection and plate tectonics are fundamental processes that control the distribution and evolution of chemical heterogeneity in the Earth's interior. One of the main mechanisms for generating chemical heterogeneity is the subduction of slabs that consist of the products (basaltic oceanic crust) and residues (harzburgite) of mid-ocean ridge melting, along with a sediment cover, into the mantle. While ancient (or "primordial") heterogeneity that results from the accretion and differentiation of our planet may have been preserved somewhere in the mantle (Ballmer et al., 2017; Mukhopadhyay, 2012; Mundl et al., 2017), much of it is thought to be processed through mantle convection and near-surface melting (e.g., Rizo et al., 2013; Christensen & Hofmann, 1994). Accordingly, most of the present-day mantle is likely a

mechanical mixture of basaltic and harzburgitic materials (and their high-pressure polymorphs), consistent with geophysical and geochemical constraints (e.g., [Hofmann, 1997](#); [Xu et al., 2008](#)). Mantle structure and differentiation is controlled by convective mixing and chemical segregation of any such heterogeneity during the long-term evolution of the Earth ([Brandenburg & van Keken, 2007](#)).

Both geochemical and geophysical observations demonstrate that Earth's mantle is heterogeneous from small to large scales (e.g., [Stixrude & Lithgow-Bertelloni, 2012](#) and references therein). For example, a large number of small-scale seismic scatters have been observed in the upper to middle layers of the lower mantle ([Kaneshima & Helffrich, 1999](#)). These scatters have mostly been attributed to the subduction and stirring of basalt, as their elastic properties agree with the expected properties of high-pressure basalt that is juxtaposed to pyrolite ([Rost et al., 2008](#)). The scale-length of the detected seismic heterogeneities is typically on the order of 10 km, which is also consistent with the typical thickness of subducted crust ([Bentham & Rost, 2014](#)). Recently, mid-scale reflectors have also been observed in the shallow lower mantle, and related to fossil subduction ([Waszek et al., 2018](#)).

Large-scale heterogeneity in the Earth's mantle is also evident from seismic observations. For example, two large low-shear-velocity provinces (LLSVP), which are 1000s km wide and ~1000

km in vertical extent, have been imaged in the lowermost mantle, one beneath the Pacific and the other beneath Africa (e.g., [Dziewonski et al., 2010](#)). Sharp gradients in seismic wave speeds at their edges ([Garnero et al., 2016](#)), an anti-correlation between shear-wave and bulk-sound velocities (e.g., [Koelemeijer et al., 2015](#)) and intrinsically high densities ([Ishii & Tromp, 1999](#)) support a compositional origin of these domains. One of the end-member hypotheses proposed for the origin of these compositional anomalies (i.e., thermochemical piles) is that basalt largely segregates from harzburgite and subsequently accumulates in the deep mantle ([Brandenburg & van Keken, 2007](#); [Christensen & Hofmann, 1994](#); [Nakagawa & Tackley, 2005](#)). Alternatively, a mixture of basalt with ancient material (e.g., magma-ocean cumulates) has been proposed in terms of LLSVP composition ([Ballmer et al., 2016](#); [Tackley, 2012](#)).

Apart from the chemical heterogeneity in the lower mantle, it has been suggested that the subducted basalt is separated from harzburgite and gravitationally trapped in the MTZ. Accordingly, segregation may sustain the formation in a basalt-enriched heterogeneous reservoir, which may have various geochemical and geophysical consequences ([Anderson, 1979](#); [Ringwood & Irifune, 1988](#)). For example, it has been suggested that some plumes may rise from the basalt-enriched reservoir in the MTZ to feed hotspot volcanism (e.g., [Allègre & Turcotte, 1985](#)), or that the accumulation of basalt in the MTZ on the backside of subducted slabs may leave an imprint on the geoid ([Karato, 1997](#)). The formation of this basalt-enriched reservoir has

86 been related to the density profile of basalt relative to pyrolite (see Fig. 1), which involves a
87 density crossover at the ringwoodite-bridgmanite phase transition at 660 km depth. While basalt
88 is denser than the surrounding mantle in the upper mantle and MTZ, it is less dense at depths of
89 660~800 km ([Hirose et al., 1999](#); [Irifune & Ringwood, 1993](#)).

90 Whether or not a basalt reservoir in the MTZ can be formed depends on the efficiency of
91 segregation of basalt from harzburgite in the subducted slab either in the MTZ or above the
92 CMB. Estimates based on analytical and simplified Newtonian sandwich models establish that
93 rheology controls segregation of mantle materials, in general, and indicate that subducted slabs
94 may be sufficiently weak for segregation of basalt from harzburgite, in particular ([Karato, 1997](#);
95 [van Keken et al., 1996](#); [Lee and Chen, 2007](#)). Fully coupled numerical models of regional
96 ([Davies, 2008](#); [Motoki & Ballmer, 2015](#); [Ogawa, 2000](#)) and global-scale mantle convection
97 ([Ballmer et al., 2015](#); [Nakagawa & Buffett, 2005](#); [Nakagawa et al., 2010](#)) support that significant
98 amounts of basalt can segregate from harzburgite and accumulate in the MTZ. However, the
99 extent of basalt accumulation as a function of physical parameters remains is poorly constrained
100 in all previous studies. Indeed, a systematic parameter study has not yet been performed to
101 quantify basalt segregation and accumulation in the deep mantle and MTZ.

In this study, we use global-scale 2D thermochemical convection models to quantify effects of mantle rheology, plate tectonic style and bulk composition on the evolution and distribution of chemical heterogeneity in the mantle. In particular, we focus on the effects of radial mantle viscosity profiles on the segregation and accumulation of basalt. We scrutinize the delivery of basalt to the MTZ and lowermost mantle, and formation of harzburgite-enriched reservoir just beneath the MTZ. Finally, we quantify the characteristic residence timescales of materials in these reservoirs.

2. Methods

We use finite-volume mantle-convection code StagYY ([Tackley, 2008](#)) to solve the conservation equations of mass, momentum and energy in a two-dimensional spherical annulus geometry of a compressible infinite Prandtl number fluid. The numerical model domain is resolved by 1024×128 cells with a radial grid refinement of up to 2 times near to the surface and CMB (i.e., ~ 10 km grid spacing). Resolution tests demonstrate that our current number of cells is sufficient to model segregation and entrainment of mantle materials (see Suppl. Fig. S1 and Appendix in Tackley, 2011). In order to track composition, five million Lagrangian tracers (~ 30 tracers per cell) are distributed in the model domain. The models take phase transitions, partial melting, time-dependent internal and basal heating, pressure and temperature-dependence of viscosity, as well

as plastic rheology into account. Kinematic boundary conditions are free slip at the top and bottom.

As in previous studies (e.g., [Nakagawa & Tackley, 2012](#)), mantle materials are described as mechanical mixtures of subducted/recycled oceanic crust and subducted/recycled oceanic lithosphere. Hereafter, we refer to these rock types as “basalt” and “harzburgite”, respectively. Basalt and harzburgite and their respective high-pressure polymorphs are the end-members of our one-dimensional compositional parameterization (see below). They represent any mafic and ultramafic lithology, respectively, that has a similar density profile and melting behavior as modeled here (e.g., Fig. 1). In this parameterization, pyrolitic mantle corresponds to a mechanical mixture of ~20% basalt and ~80% harzburgite ([Xu et al., 2008](#)). End-members basalt and harzburgite are defined as a solid solution of olivine (ol) and pyroxene-garnet (px-gt) mineral systems (harzburgite: 75% ol and 25% px-gt; basalt: 100% px-gt). Each of these systems is parameterized to undergo the relevant solid-state phase transitions (see Suppl. Table S1). The density profiles of mantle materials are then calculated from our parameterization of major phase transitions, and the thermodynamic parameters of each phase. These density profiles, as shown in Figure 1, are consistent with those derived by [Xu et al. \(2008\)](#).

We apply a strongly temperature and pressure-dependent rheology using an Arrhenius-type formulation:

$$\eta_{viscous}(T, p) = \prod_{ij} \lambda_{ij}^{f_j \Gamma_{ij}} \eta_0 \exp\left(\frac{E+pV}{RT} - \frac{E}{RT_0}\right) \quad (1)$$

where η_0 and T_0 are the reference viscosity and reference temperature (i.e., at the surface at zero pressure), respectively; E is activation energy; p is pressure; V is activation volume; T is absolute temperature, and R the ideal gas constant; Viscosity jumps are imposed at the phase transitions as suggested by mineral physics experiments and theoretical calculations (e.g., [Ammann et al., 2010](#)). λ_{ij} is the viscosity jump caused by phase transition (i, j) (see Suppl. Table S1), f_j is the fraction of phase system j (olivine or pyroxene-garnet), Γ_{ij} is the phase function for each phase ([Nakagawa & Tackley, 2010](#)). The relevant viscosities in each mantle layer are free model parameters in this study (see below).

In order to obtain plate-like tectonic behavior, plastic yielding is included using a Drucker-Prager yield criterion with a pressure-dependent effective yield-stress parameterization:

$$\eta_{yield} = \frac{C+p\mu}{2\varepsilon_{II}} \quad (2)$$

where μ is the friction coefficient, C the cohesion coefficient and ε_{II} the second invariant of the strain rate tensor. The effective viscosity is defined by the minimum of the two components from equation (1) and (2):

152 $\eta_{eff} = \min(\eta_{viscous}, \eta_{yield})$ (3)

153 Partial melting generates basaltic oceanic crust and a complementary depleted residue. At each
154 time step, the temperature in each cell is compared to the solidus temperature. As long as the
155 temperature in a specific cell exceeds the solidus, melt is generated to bring the temperature back
156 to solidus, leaving a residue behind with a depletion that depends on the related degree of
157 melting. For details, see [Nakagawa & Tackley \(2010\)](#) and references therein.

158 The initial condition for temperature is an adiabatic temperature profile with a potential
159 temperature of 2000 K with thermal boundary layers at the top and bottom of the model box. The
160 surface temperature is set at 300 K. The initial CMB temperature is assumed to be 5913 K. The
161 core cools as heat is extracted by the mantle as in [Nakagawa & Tackley \(2010\)](#). Internal heating
162 is also time-dependent, initially being H_r and decaying according to a timescale τ , which is
163 similar to the characteristic half-life of the dominant heat-producing radionuclides in the Earth's
164 mantle. Our models are initialized with homogeneous composition, i.e., in most cases with
165 pyrolitic composition, which corresponds to a mechanical mixture of 20% basalt and 80%
166 harzburgite in most of our models.

167 All physical parameters used in the model are listed in the Suppl. Table S2. Hereinafter, we refer
168 to basalt fraction (compositional index) as X_{BS} . This simplified compositional index is a

projection of multi-oxide mantle rock composition on one single axis, and defined to range from 0 (harzburgite) to 1 (basalt), with pyrolite being ~0.2.

3. Results

3.1. Model predictions for the reference case

Before exploring the parameter sensitivity of our models, we first describe in detail the distribution and evolution of chemical heterogeneity in our reference model (for initial temperature and viscosity profiles, see Suppl. Fig. S2-3). The reference case is characterized by a viscosity jump of a factor 30 at 660 km depth, but no viscosity jump at 410 km depth (for other relevant parameters, see Suppl. Table S2). Due to our visco-plastic rheology, slabs of basalt and harzburgite are continuously introduced into the mantle at various subduction zones over 4.5 Gyr model time.

Despite whole-mantle convection, compositional layering is predicted to occur across the mantle over large regions (Fig. 2). A basalt-enriched reservoir is commonly formed over large regions at the base of the MTZ (i.e., just above 660 km depth), and a complementary harzburgite-enriched reservoir is formed just below 660 km depth. In addition, large-scale heterogeneous thermochemical piles accumulate at the base of the mantle. On top of these strongly-enhanced reservoirs visible in Figure 2, the average radial profile of basalt fraction X_{BS} (Fig. 3a) shows that

the composition of the uppermost mantle is generally shifted toward harzburgite, while most of the lower mantle is relatively enhanced in basalt (see section 3.4). The formation of this global compositional layering in the presence of mantle convection requires segregation of basaltic materials from depleted harzburgitic, and is ultimately controlled by the density profiles in Figure 1. In general, compositional segregation competes with convective stirring (i.e., mechanical mixing) in the convecting mantle.

Figure 3b shows that the mantle geotherm of the reference case is generally subadiabatic. Subadiabatic geotherms are typical for whole-mantle convection models (Sinha & Butler, 2007), in which plumes rise to feed the uppermost mantle, and slabs sink to the base of the mantle (Fig. 2f). On top of a generally subadiabatic geotherm, there are potential-temperature minima and maxima in and just below the MTZ, respectively, over most of mantle evolution. We attribute these minima and maxima to slabs that stagnate at 660 km depth, and warm harzburgite that accumulates just beneath, respectively. We also note that the predicted mantle temperatures are ~200 K higher than realistic, which may be due to the distribution of internal heat sources (see Suppl. Fig. S4).

Segregation of mantle rock types and the related large-scale layering of small-scale heterogeneity are promoted by the density difference between harzburgitic and basaltic materials as a function

of depth (Fig. 1). Models predict that the first segregation of basalt from harzburgite (i.e., within the subducted slab) usually occurs in the hot thermal boundary layer near the CMB, where the viscosity is lowest (also see [Karato, 1997](#); [Tackley, 2011](#)). Note that decreasing viscosities tends to promote segregation of short-length heterogeneity as the growth rate and wavelength of Rayleigh-Taylor instability is reduced. Subsequently, larger blobs of basalt are transported by mantle convection (e.g., plumes), and ultimately accumulate in a given layer based on the well-constrained density profile in Figure 1. Basalt is denser than pyrolite and harzburgite through most of the mantle, and hence tends to accumulate in the lowermost mantle. In turn, harzburgite tends to accumulate in the upper mantle. Accumulation of basalt in the MTZ is explained by the density crossover that occurs at the base of the MTZ (there is no such accumulation in a test case without density crossover; see Fig. 3c-d). Since basaltic materials are less dense than the surrounding mantle at depths of 660-720 km (Fig. 1), they tend to be gravitationally trapped in the MTZ. Conversely, harzburgitic materials tend to be trapped just below the MTZ (see arrows in Fig. 1).

In more detail, our reference model predicts that deep-rooted plumes as well as stagnant slabs transport basalt to the MTZ in order to establish the basalt-enriched reservoir. At early model times $< \sim 0.5$ Gyr, subducted slabs play the major role in transporting basalt to the MTZ. Due to the viscosity and density jump at the ringwoodite-to-perovskite phase transition (i.e., coupled

with its negative Clapeyron slope) at 660 km depth, the cold and strong slabs stagnate in the MTZ and subsequently become warm and weak as they are heated. This heating promotes the segregation of basalt from harzburgite (Motoki & Ballmer, 2015), in this case directly in the MTZ. Apart from stagnant slabs in the MTZ, many subducted slabs penetrate through the MTZ and sink into the deep mantle. As they reach the deep mantle, basaltic components segregate from harzburgite near the CMB, and subsequently accumulate above the CMB, forming the first basalt-enriched thermochemical piles (Fig. 2a-b), which subsequently grow (Fig. 2c). At later model times (i.e., $> \sim 0.5$ Gyr), the mantle lithosphere becomes stronger as the mantle (and core) progressively cool(s). This strengthening tends to make subduction less efficient, resulting in slower plate speeds, fewer subduction zones, and larger plate thicknesses. In this phase, basalt is most efficiently delivered by plumes to MTZ due to entrainment from thermochemical piles. Chunks of basalt are “lost” by plumes to accumulate in the MTZ, because of its large density anomaly (Fig. 1) as well as the relatively low viscosity in the MTZ.

In addition to the transport of basalt to the MTZ by plumes (and slabs), the balance of basalt in the MTZ is controlled by processes for basalt removal. Episodic removal of basalt from the MTZ is accomplished by three mechanisms. First, downgoing subducted slabs can entrain materials that accumulate in or at the base of the MTZ, thus potentially “cleaning out” any regional basalt-enriched reservoir (along with the underlying harzburgite-enriched reservoir). This mechanism is

dominant among the three mechanisms, especially at relatively late model times ($> \sim 0.5$ Gyr). Second, large mantle plumes can likewise entrain (or push out) any layered material from (the base of) the MTZ. Third, as the basalt-enriched layer grows beyond a critical thickness, it becomes gravitationally unstable and promotes diapiric basaltic avalanches (encircled by white ellipses in Fig. 2d-e). Nevertheless, as basalt is continuously delivered to the MTZ, regional reservoirs can be sustained for long model times, and e.g., just be swept laterally, mostly maintaining isostatic equilibrium. Hence, the global basalt profile soon reaches (after ~ 0.5 Gyrs) and maintains a statistical steady state (Fig. 3a).

To quantify the distribution of heterogeneity in the mantle, Figure 4a-b shows histograms of average X_{BS} (and corresponding basalt and harzburgite enrichment) in layers just above and just below 660 km from 2 to 4.5 Gyr. Just above 660 km depth, X_{BS} is widely 30%~50%, corresponding to basalt enrichments (relative to pyrolite) of 12%~37% (Fig. 4a). However, there are also some strongly-enriched ($X_{BS} \gg 50\%$) and pyrolitic ($X_{BS} \approx 20\%$) regions. In turn, the dominant volume of the layer just below 660 km depth displays $X_{BS} \approx 10\%$, corresponding to harzburgite enrichments of 40%~80%. Fig. 4c shows that the volume of basalt-enriched piles remains nearly constant over the last 2.5 Gyr.

Finally, Figure 4d-f shows the distributions of basalt/harzburgite ages for the relevant reservoirs in/beneath the MTZ and above the CMB. The dominant basalt and harzburgite ages in both basalt-enriched and harzburgite-enriched reservoir are ~ 2 Gyr. This can be seen as a rough timescale for the delivery of materials to plus their residence time in these reservoirs. Only small volumes of the basalt-enriched reservoir are younger than 1 Gyr, which is an indicator of the minor role of delivery by young subducted slabs. In turn, the basalt-age distribution across the depth range of 2390-2890 km is bimodal (Fig. 4f): young subducted basalt (< 1 Gyr) with dominant ages of ~ 0.5 Gyr and old subducted basalt (> 2 Gyr) with dominant ages of ~ 2.5 Gyr (the latter mostly comprising thermochemical piles). That basalt-enriched piles can survive for billions of years is consistent with previous work (e.g., [Mulyukova et al., 2015](#)). Note that the harzburgite reservoir in the uppermost lower mantle also displays a bimodal distribution (Fig. 4e), but the basalt reservoir in the MTZ does not (Fig. 4d). This result highlights the segregation of basalt from harzburgite in the lower mantle. Whereas both young and old harzburgite can be delivered to the reservoir beneath the MTZ due to its intrinsic buoyancy, only old basalt is delivered to the MTZ. Before delivery, basalt is stored in thermochemical piles to be heated and overcome its intrinsic density anomaly, and eventually be entrained by plumes.

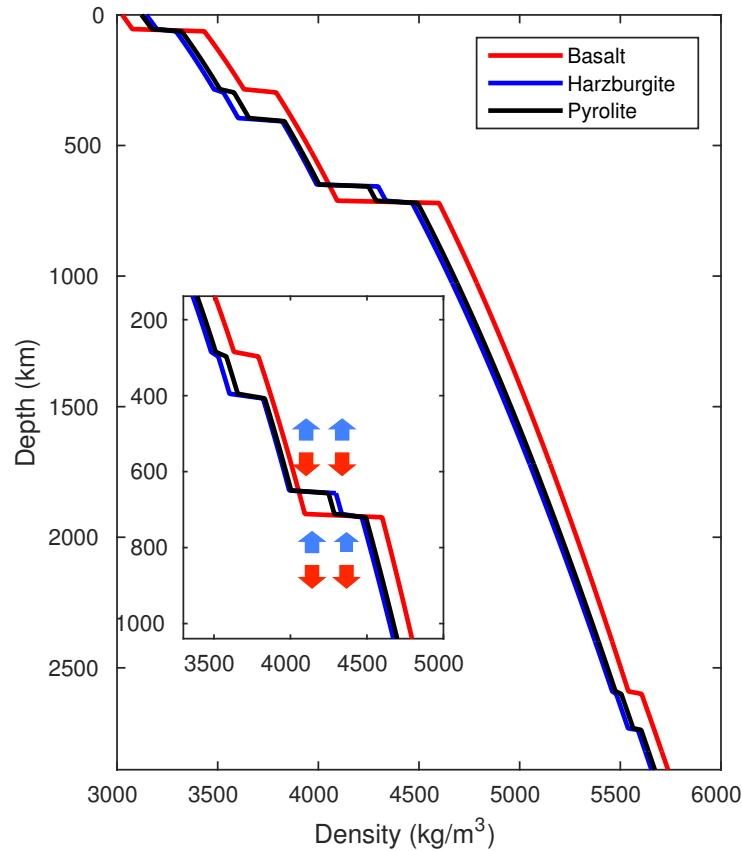


Fig. 1. Density profiles for basalt (100% pyroxene-garnet), harzburgite (75% olivine + 25% pyroxene-garnet) and pyrolite (20% basalt + 80% harzburgite). Note the density crossover between 660 and 720 km. We parameterize the gradual breakdown of garnet (Hirose et al., 1999; Irifune & Ringwood, 1993) as a transition of width 75 km (see Suppl. Table S1) at 720 km depth. The red and blue arrows denote the negative and positive buoyancy of basalt and harzburgite away from this crossover region, respectively.

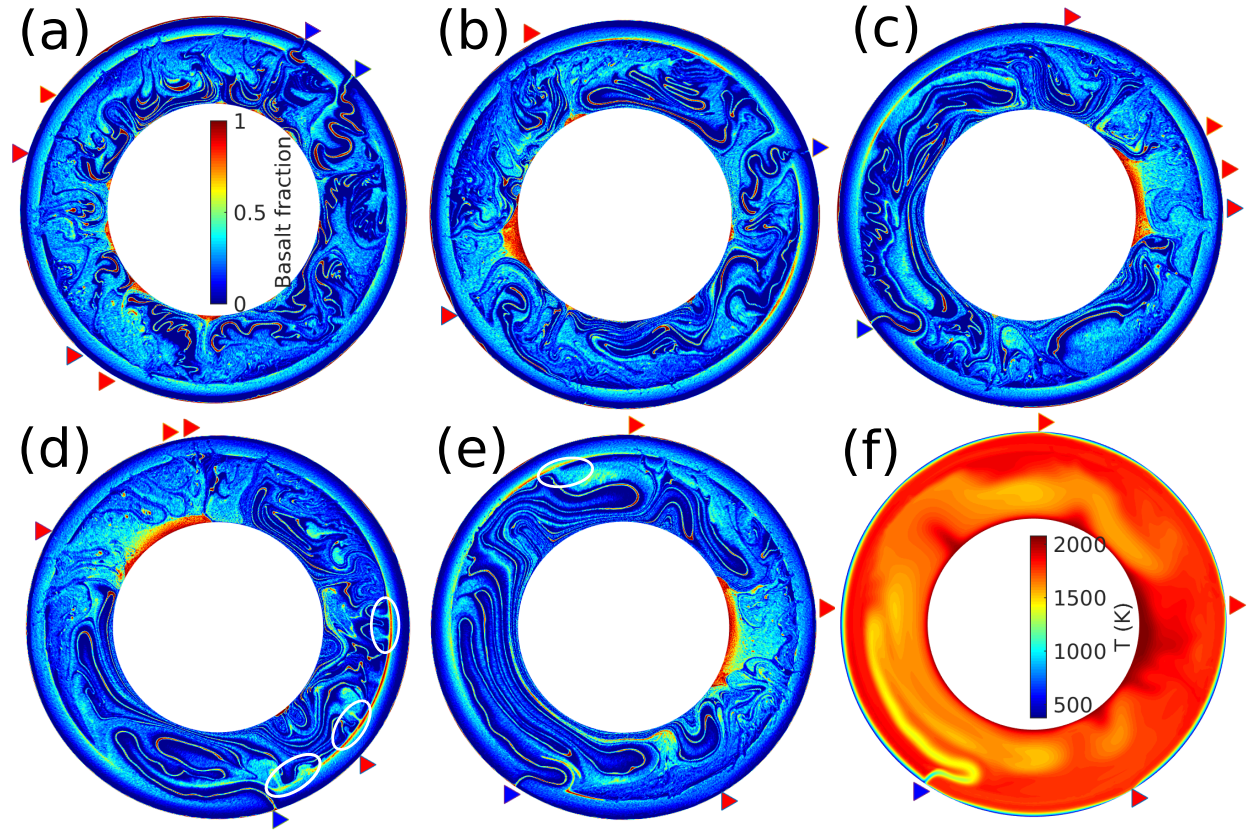


Fig. 2. Snapshots of X_{BS} (compositional index) at model times (a) 1.0 Gyr (b) 2.0 Gyr (c) 3.0 Gyr (d) 4.0 Gyr (e) 4.5 Gyr; (f) potential temperature T at 4.5 Gyr for the reference model. Blue and red triangles refer to subduction zones and mid-ocean ridges, respectively. White ellipses denote the diapiric basaltic avalanches. Rising plumes are readily identified in panel (f). For movies of the compositional and thermal evolution of the reference case, we refer the reader to the supporting online information (Suppl. Movie S1).

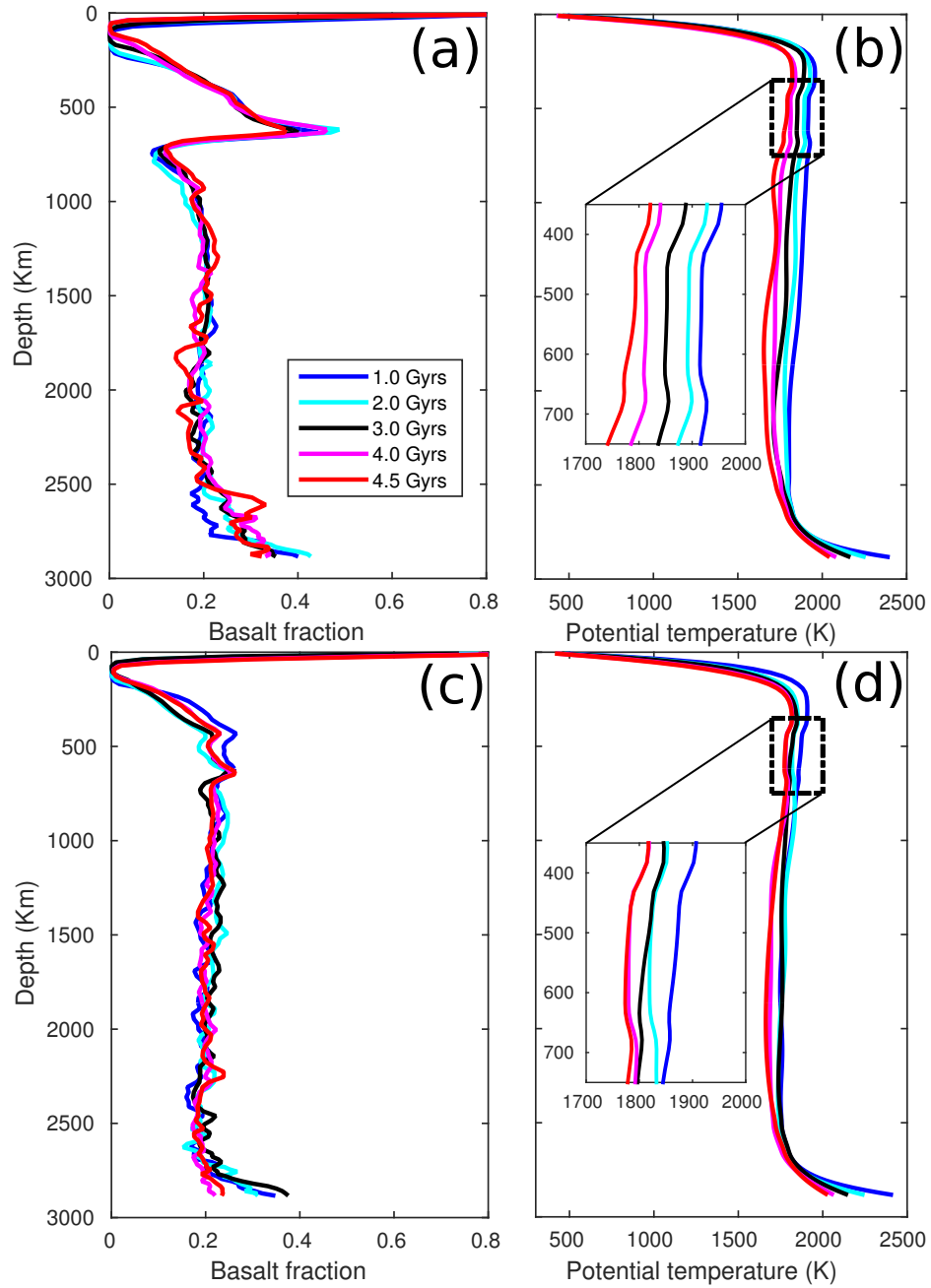
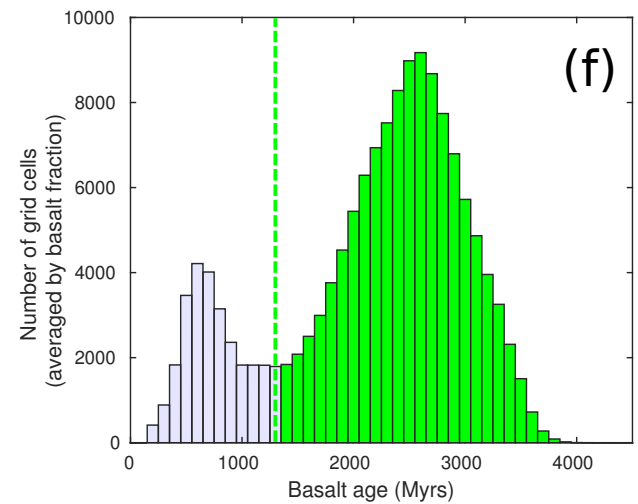
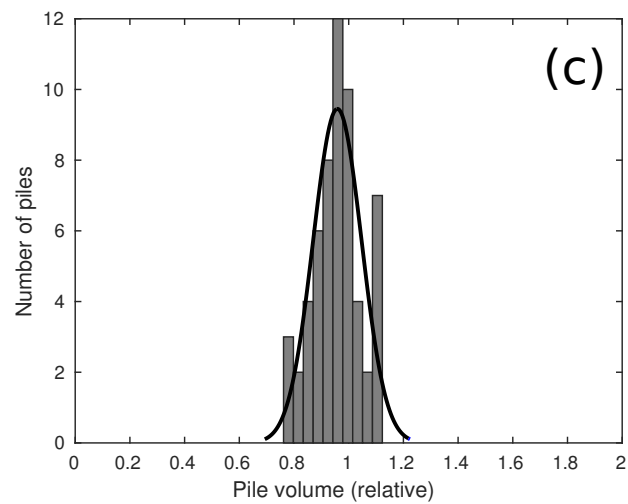
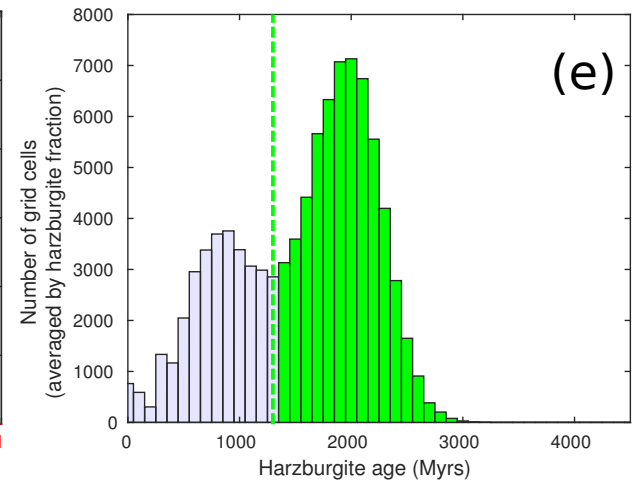
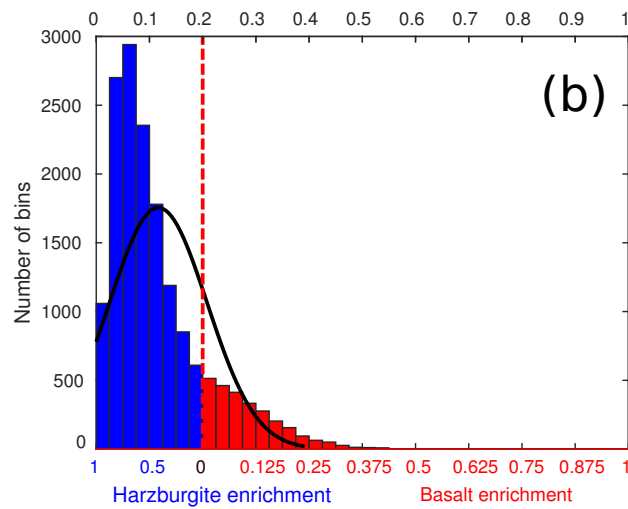
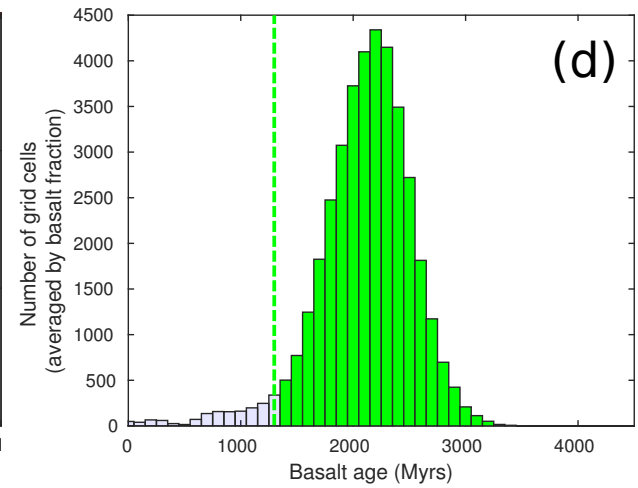
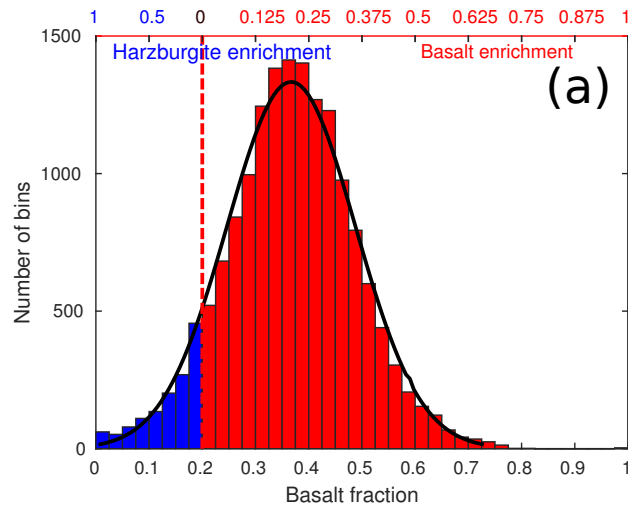


Fig. 3. Radial average profiles of (a) X_{BS} (compositional index) and (b) potential temperature for the reference case at different model times (from 1.0 to 4.5 Gyr as labeled). For comparison, (c) X_{BS} (compositional index) and (d) potential temperature for a test case, in which the density crossover at 660-720 km depth is artificially switched off (i.e., the depth of the phase change in

291 the px-gt system is set to 660 km instead of 720 km). In this test case (with otherwise the same
292 parameters as for the reference model), no basalt-/harzburgite-enriched reservoir is formed just
293 above/beneath 660 km. Note detailed potential-temperature gradients across the MTZ as shown
294 in insets.

295



296

297

Fig. 4. Distribution of heterogeneity (i.e., in terms of X_{BS} , basalt age and relative volume) in the MTZ (i.e., at depths of 560-660 km, a and d), just beneath the MTZ (i.e., at depths of 660-760 km, b and e), and above the CMB (i.e., at depths of 2390-2890km, c and f). Note that the black curve in each histogram is the corresponding normal distribution, plotted for reference. Red and green vertical lines denote the boundaries between basalt enrichment and harzburgite enrichment, and between relatively young and old reservoirs, respectively. For each bin (~ 3 degrees wide) in panels (a-b), composition is averaged over the depth range labeled. Bins are summed into histograms over model times 2-4.5 Gyr, scaled by (a) X_{BS} , or (b) $1-X_{BS}$. In (c), pile volumes are measured over 2-4.5 Gyr, and normalized by that in the last time-step of the reference case (Figure 2e). In (e-f), basalt ages at grid cells are summed into histograms over 3.5-4.5 Gyr.

3.2. *Effects of mantle viscosity*

To investigate the influence of mantle viscosity on the segregation and accumulation of basalt in the mantle, we systematically vary three model parameters: (1) the viscosity jump due to the phase change at 410 km; (2) the viscosity jump due to the phase change at 660 km; and (3) the reference viscosity. Combining these three parameters, we generate four groups of radial mantle viscosity profiles (see Suppl. Fig. S3). In each of these four groups, the viscosities are varied by

up to a factor of ~ 100 in (A) the uppermost mantle (i.e., at depths < 410 km), (B) the MTZ (i.e., at depths of 410-660 km), and (C) the lower mantle (i.e., at depths > 660 km), and (D) the whole mantle, respectively.

In group A, our results suggest that relatively high uppermost-mantle (plus lithospheric) viscosities have no or little effects on the accumulation of basalt in the MTZ (Fig. 6a), while they tend to result in larger harzburgite-enriched reservoir beneath the MTZ and higher amounts of basalt above CMB (see e.g., Figs. 5a, 6e and 6j). Models show that relatively high uppermost-mantle viscosities are associated with thicker plates and larger crustal thicknesses (see Suppl. Figs. S7a and S8a). The related thicker subducted slabs promote segregation of basalt from harzburgite in the lower mantle, ultimately leading to larger amounts of harzburgite just beneath the MTZ (Fig. 6e) and larger basalt-enriched piles above the CMB (Fig. 6j). Besides, thicker plates also result in slower plate velocities (i.e. root-mean-square velocity at the surface) and lower plate mobilities (see Suppl. Figs. S5a and S5e), hence inhibiting mantle and core cooling (see Suppl. Figs. S6a and S6e), thereby promoting partial melting, resulting in a more depleted uppermost mantle (i.e., less X_{BS} in Fig. 5a). In turn, relatively low uppermost-mantle viscosities are associated with thinner plates. While segregation of thinner subducted slabs is inefficient in the deep mantle; this is not the case in the upper mantle and MTZ. Thinner slabs tend to stagnate more readily in the MTZ since they are relatively weak, and segregate there into their basaltic

and harzburgitic components as they are warmed up. This effect trades off with the negative effect of slab (or subducted crustal) thicknesses on segregation in the lower mantle. Therefore, uppermost-mantle viscosities do not have obvious effects on the amount of basalt-enriched reservoir in the MTZ.

In group B, our models show that the X_{BS} in the MTZ is systematically controlled by MTZ viscosity (see Figs. 5b and 6b). However, this control is not very strong: the final average X_{BS} in the MTZ ranges between 30% and 37% in all cases of Group B (Fig. 5b). Besides, we find that relatively low viscosities in the MTZ (and a related large viscosity jump at the 660 km) tend to increase the resistance of the mantle to slab sinking, which leads to a relatively large amount of basalt accumulated in the MTZ from 1 to 2 Gyr. For relatively high viscosities in the MTZ, models predict instead that X_{BS} in the MTZ is relatively low throughout the entire history of mantle evolution. The variation of viscosities in the MTZ has little or no effects on the volume of basalt piles that accumulate above the CMB (Fig. 6k), or on the harzburgite-enriched reservoir just beneath the MTZ (Fig. 6f). An exception is that the volume of piles is somewhat increased for very low MTZ viscosities (such as case B1), as the efficiently segregated basalt in the MTZ ultimately reaches the CMB.

In group C, our models predict that the harzburgite-enrichment beneath the MTZ (Fig. 6g) as well as the volume of basalt-enriched piles above the CMB (Fig. 6l) increase with decreasing lower-mantle viscosity. This result is well explained by the effects of mantle viscosity on the efficiency of segregation. Any harzburgite segregated in the lower mantle tends to rise and eventually accumulate just below 660 km depth, and any segregated basalt tends to sink and eventually accumulate above the CMB. In turn, X_{BS} in the MTZ is largely independent of (i.e., only very slightly increases with) lower-mantle viscosity (see Figs. 5c and 6c). We attribute this result to a trade-off: while inhibiting segregation of basalt in the deep, higher lower-mantle viscosities tend to stabilize the conduits between convection cells, which facilitates the entrainment of basalt through these conduits (see Suppl. Movie S2-3). Moreover, higher lower-mantle viscosities tend to promote slab stagnation in the MTZ by increasing the viscosity jump at the 660. In combination, these two effects result in a slightly stronger enhancement of basalt in the MTZ (Fig. 5c, case C4), which confirms that both slabs (from above) and plumes (from below) deliver basalt to the MTZ.

In group D, we find that relatively low whole-mantle viscosities tend to enhance the segregation of basalt from harzburgite, promoting the enhancement of basalt in the MTZ (Fig. 6d) and deep mantle (Fig. 6m), as well as that of harzburgite just beneath the MTZ (Fig. 5d, 6h). This result can be explained by the combination of all effects discussed above. For example, for relatively

low whole-mantle viscosities, enhancement of basalt in the MTZ already occurs at early model times, and remains rather stable over billions of years with small second-order variations (see Suppl. Movie S1 and S4). These variations reflect the partial destruction of any basalt-enhanced layer in the MTZ (e.g., by sinking slabs), and subsequent replenishment. Similar to group C, lower whole-mantle viscosities promote segregation in the deep mantle to sustain large piles (see Fig. 6m). The formed piles are able to survive for several billions of years as any entrainment is usually (over)compensated by continued addition of basalt through segregation.

Despite the aforementioned variations, we stress that the predicted basalt contents (i.e., X_{BS}) in the MTZ are fairly robust over a wide range of viscosity profiles. While relatively low local mantle viscosity can promote the segregation and accumulation of basalt in the MTZ, average X_{BS} in the MTZ range from 0.3 to 0.35 (i.e., corresponding to 12.5%–18.7% basalt enrichment) for most cases, and up to 0.4 only for a few cases (see Figs. 6a-d). While for some cases (A4 and D4), the predicted average X_{BS} are < 0.3 , these cases are not Earth-like, because of very small CMB heat fluxes and plate velocities (see Suppl. Figs. S5-6).

Similarly, the average harzburgite content (i.e., $1-X_{BS}$) in the thin layer just below 660 km depth is mostly parameter-independent. It is just sensitive to the viscosity in the lower mantle, as is explored in groups C and D. Furthermore, it slightly varies with parameters that control slab

thickness, such as uppermost-mantle viscosity. Nevertheless, the average harzburgite enrichment at 660-760 km depth of most cases (except cases that are not Earth-like as mentioned above) just varies between 25% to 50%, which corresponds to with $10\% < X_{BS} < 15\%$ (Figs. 6e-h).

In turn, the volume of piles above the CMB is strongly sensitive to the mantle viscosity profile (Figs. 6j-m). Some cases result in no piles at all while other cases lead to very large pile volumes that are about twice as large as in the reference case (see Fig. 2e). This result is well explained by a variable balance between segregation and entrainment across cases in the context of a quasi-infinite capacity of the deep-mantle reservoir (i.e., little or no feedback between pile volumes and entrainment). The efficiency of segregation is controlled by the local (i.e., lower-mantle) viscosity, and the thickness of the delivered basaltic slabs.

Overall, two processes occur in the mantle: segregation and accumulation. Segregation of basalt from harzburgite is a prerequisite for the subsequent accumulation of basalt in/near the MTZ/CMB (or of harzburgite just below the MTZ). Our models suggest that the balance between delivery and removal controls the content of basalt/harzburgite in various mantle reservoirs. Delivery and removal are controlled by the scale-length of heterogeneity and the local viscosity, and thereby parameter-dependent. That the basalt content in the MTZ is robust over a wide range of parameters is explained by the variety of processes that deliver basalt to the MTZ

(mostly plumes, but also stagnant slabs), and remove basalt from the MTZ (mostly sinking slabs). These processes do not depend on the same parameters. Importantly, any process for removal becomes more efficient as the MTZ is more enriched in basalt. Thus, the MTZ basalt contents are ultimately controlled by its capacity. In contrast, the harzburgite layer just below 660 km depth gets mostly replenished by just one process (i.e., harzburgite rising through the lower mantle), the efficiency of which depends on various parameters, mostly lower-mantle viscosity (see above). We highlight that our models robustly predict that the MTZ is enriched in basalt, and constrain the typical degree of enrichment as $\sim 15\%$ relative to pyrolite (i.e., $0.3 < X_{BS} < 0.35$). All models display a subadiabatic potential-temperature gradient across the MTZ.

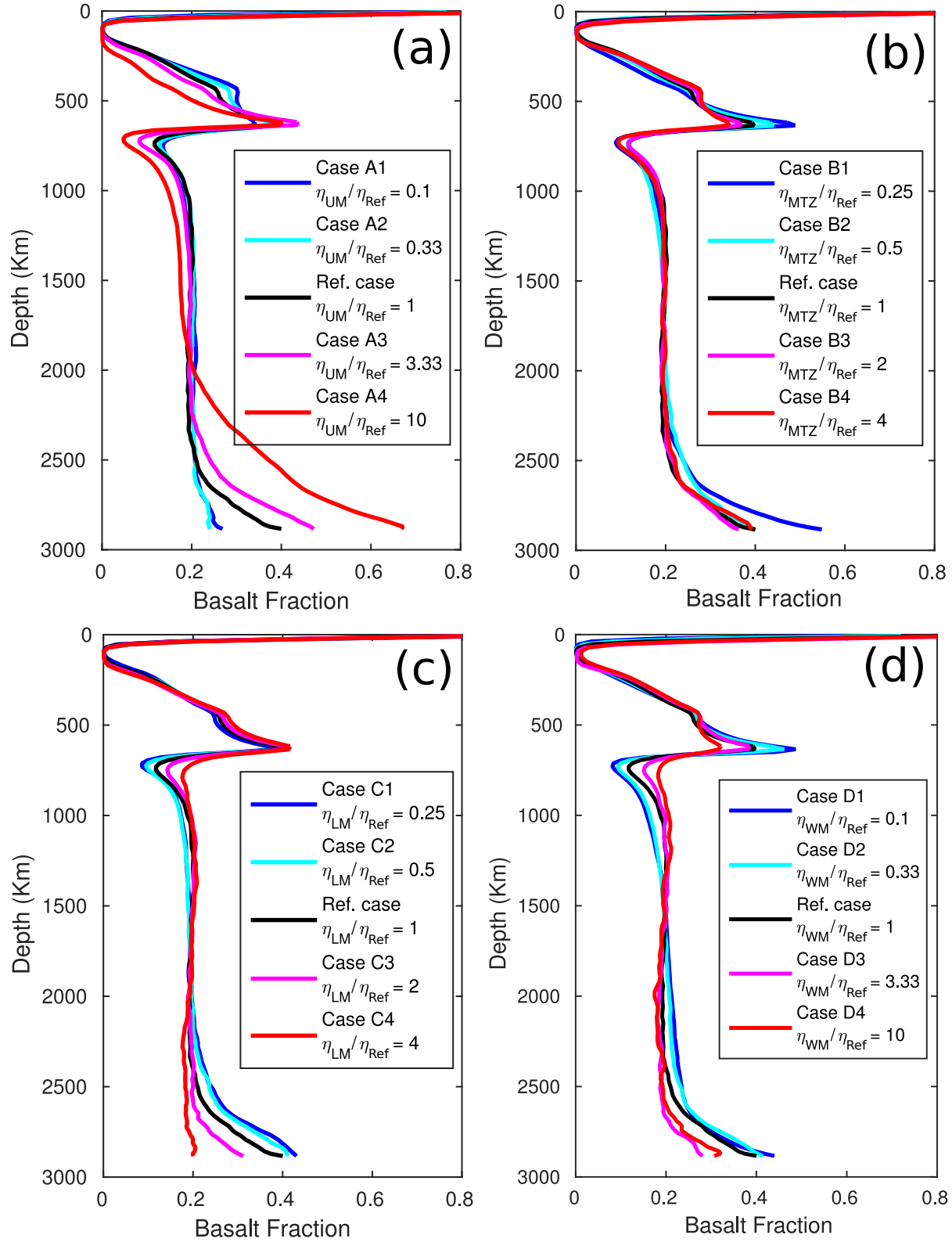


Fig. 5. Radial profiles of X_{BS} (compositional index), averaged laterally and over time (i.e., between 2 and 4.5 Gyr) for (a) group A: the uppermost-mantle (UM) viscosity (b) group B: MTZ

viscosity (c) group C: the lower-mantle (LM) viscosity (d) group D: the whole-mantle (WH) viscosity. Note that η_{UM} , η_{MTZ} , η_{LM} and η_{WM} denote uppermost-mantle viscosity, MTZ viscosity, lower-mantle viscosity, and whole-mantle viscosity, respectively. Correspondingly, η_{Ref} denotes the viscosity of the reference case.

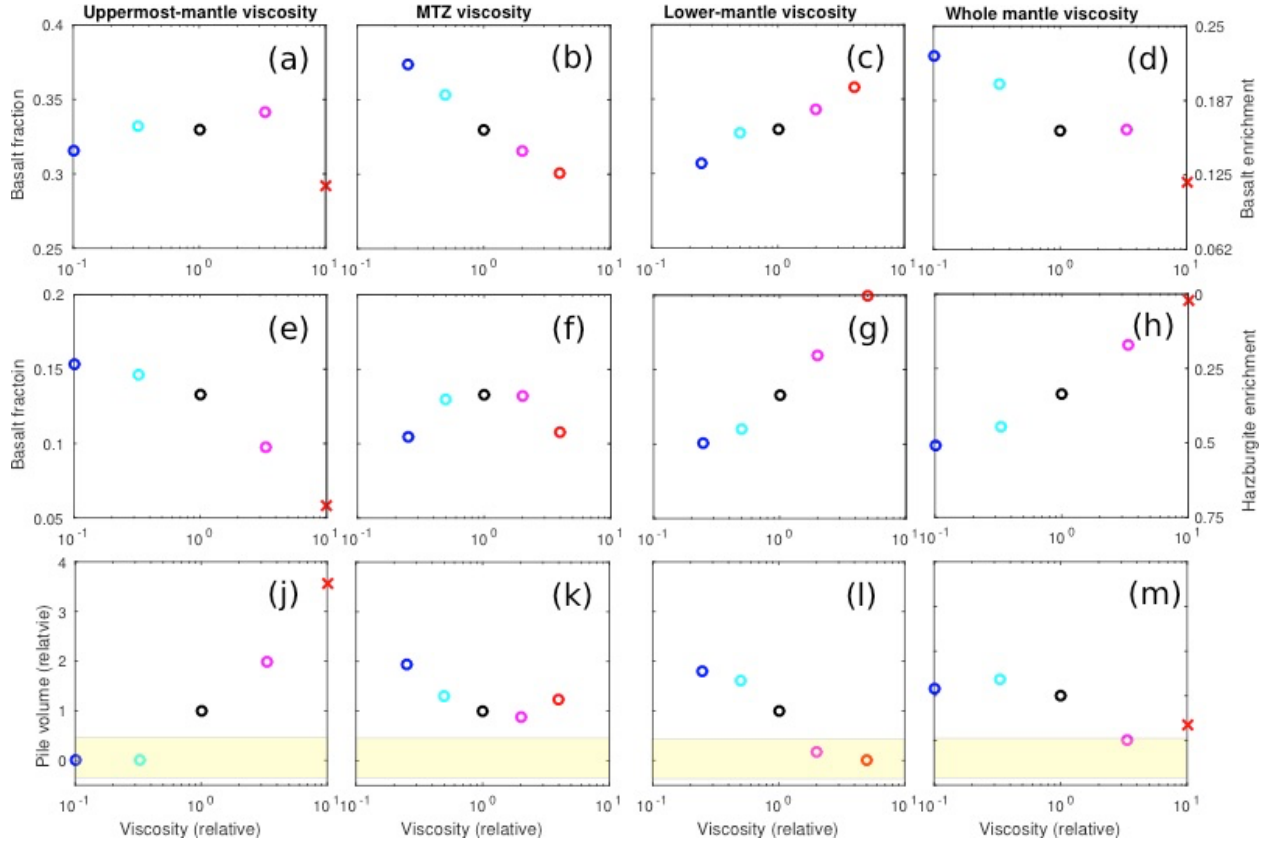


Fig. 6. Parameter sensitivity of the predicted composition of mantle layers. (Top row) Basalt fraction X_{BS} (compositional index), and corresponding basalt enrichment relative to pyrolite in the MTZ (i.e., at depths of 560-660 km), averaged laterally and over time (i.e., from 2 to 4.5 Gyr) for all cases in groups A-D (from left to right columns). (Middle row) X_{BS} and corresponding harzburgite enrichment just beneath the MTZ (i.e., at depths of 660-760 km) for all cases in

groups A-D. (Bottom row) relative volume (i.e., relative to the pile volume of the reference case at 4.5 Gyr (see Fig. 2e)) of basalt-enriched thermochemical piles (i.e., the threshold value of $X_{BS} > 30\%$ is used to discriminate piles and ambient mantle composition) above the CMB (i.e., at depths of 2590-2890 km). Crosses denote cases that do not match our criteria for Earth-like tectonic style (see Suppl. Fig. S5-6). The light yellow area shows cases with very small or no piles. For colors, see Fig. 5 legend.

3.3. *Effects of plate-tectonic style*

Next, we investigate the effects of an important but poorly constrained parameter for tectonic behavior of planets: the effective yield stress. While relatively low values sustain plate-tectonic behavior, large values promote the formation of a stagnant lid (e.g., [Nakagawa & Tackley, 2015](#)). We vary the effective yield stress by systematically changing the friction coefficient μ between 0.005 and 0.08 (see eq. 2 and 3). As we explore the effective yield stress, we keep all other parameters, including the viscosity profile, fixed.

We find that the activity of tectonics systematically varies within the relatively narrow range of friction coefficients μ explored here. For example, for the case E4 with the highest $\mu = 0.08$, plate tectonics remains episodic with intermittent episodes of stagnant-lid tectonics (i.e., plate

mobility is episodically zero). All other cases display persistent plate tectonics. We find that the number of subduction zones and, plate mobility, and average speed of tectonic plates increase with decreasing yield stress (Fig. 7a). Therefore, more slab material is conveyed into the mantle for small yield stresses, promoting planetary cooling, and ultimately reducing the extents of basalt melting (see Fig. 7c where case E1 and E2 are featured with less depleted upper mantle). Accordingly, crustal thicknesses are smaller for lower yield stresses. The related more active subduction and sinking of (thinner) slabs continuously cleans out the MTZ through time such that for case E1 stable basalt-enriched reservoir in the MTZ cannot be established at all (Fig. 7b). Slab thicknesses and crustal thicknesses also have a strong effect on the segregation of heterogeneity in the lower mantle. Similar to results in group A, higher yield stresses associated with thicker subducted slabs result in larger basalt-enriched piles above the CMB (Fig. 7c). Another effect involves the influence of planetary cooling as a function of yield stress on mantle viscosity, and thereby on the distribution of heterogeneity (i.e., again in analogy to group A above). Finally, it should be noted that there is a visible accumulation of basalt in the MTZ, delaminated from the base of the crust in a stagnant lid regime ([Armann & Tackley, 2012](#); [Nakagawa & Tackley, 2015](#)) with high yield stress. That all said, we stress that neither relatively low (case E1) nor high (case E4) yield stresses are relevant for the Earth. This further confirms that the yield stress used in our reference case (and all other cases in groups A-D and F) is

reasonable for generating Earth-like plate tectonics, although there remains uncertainty in terms of this parameter.

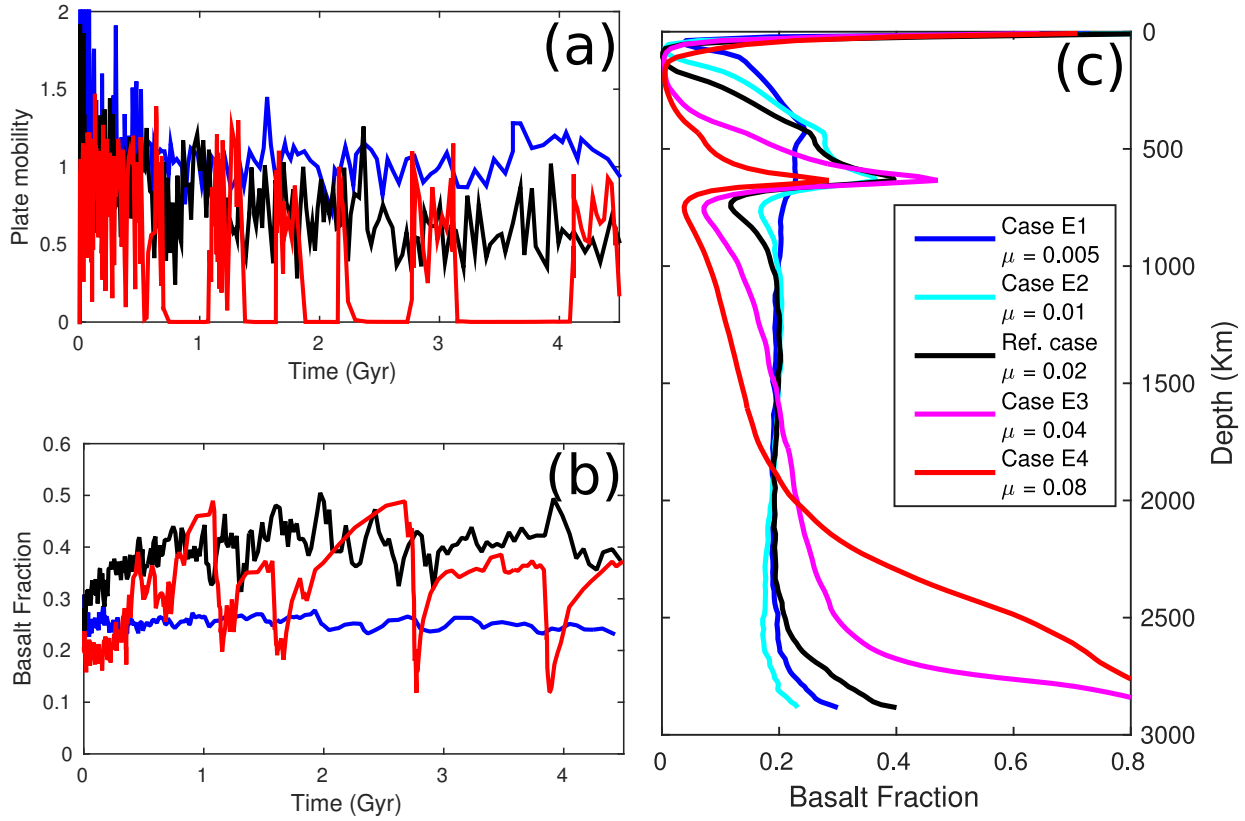


Fig. 7. (a) Plate mobility, (b) radial average X_{BS} (compositional index) in the MTZ from 0 to 4.5 Gyr, and (c) radial average X_{BS} (compositional index) between 2 and 4.5 Gyr for cases with the different friction coefficient μ .

3.4. Effects of initial mantle composition

Finally, we investigate the influence of initial mantle composition on the distribution of heterogeneity in the mantle. We vary the initial X_{BS} of the mantle, from 0.25 to 0.4. Thereby, the bulk composition of the silicate Earth is shifted towards that of basalt. In general, it is accepted that the source of MORB melting (i.e., the uppermost mantle) consists of pyrolite, which is similar to the rock type peridotite (Ringwood, 1975), and corresponding to $X_{BS} = 0.2$. However, the radially averaged basalt profiles of all models discussed above (including the reference case), which all have an initial and bulk X_{BS} of 0.2, predict that the upper mantle is depleted in basaltic components relative to pyrolite.

As we vary the initial X_{BS} in this suite (all other parameters are fixed at reference values), we find that the radially averaged basalt profiles are shifted as a whole towards higher basalt fractions (Fig. 8). Accordingly, the average upper-mantle X_{BS} is also shifted. Obviously, case F4 is not Earth-like, since its radially averaged X_{BS} in the asthenosphere (see dashed red line in the yellow box in Fig. 8) is quite a bit higher (i.e., $X_{BS} = 0.26$) than that of pyrolite (i.e., $X_{BS} = 0.2$). In turn, cases F2 and F3 display asthenospheric average compositions similar to pyrolite ($X_{BS} = 0.18$ and 0.22, respectively). In these cases, the bulk lower mantle is significantly shifted towards higher basalt contents than pyrolite (see dashed lines in the green box in Fig. 8). In addition, the MTZ and lowermost mantle (thermochemical piles) display significant basalt reservoirs. Due to the significant enhancement of mafic (SiO_2 -rich) basalt in case F3, even the shallow lower mantle

(660-1500 km depth, green box in Fig. 8) is mostly silicate perovskitic (bridgmanitic) on average with a molar Mg/Si-ratio of 1.08 (i.e., calculated based on Table 1 in [Xu et al., 2008](#)). At 1500 km depth, the average molar Mg/Si ratio is ~ 1.07 and ~ 1.00 in cases F2 and F3, respectively. According to our models, if indeed significant reservoirs of basalt exist in the MTZ and lower mantle, the composition of the bulk-silicate Earth may be shifted towards basalt relative to the uppermost-mantle composition of pyrolite, being more similar to the starting compositions of cases F2 or F3. Accordingly, our previous estimation of $0.3 < X_{BS} < 0.35$ in the MTZ may be a lower bound. Along these lines, segregation of basalt from harzburgite can help to filter heterogeneity in order to sustain large-scale mantle layering, even in the presence of whole-mantle convection.

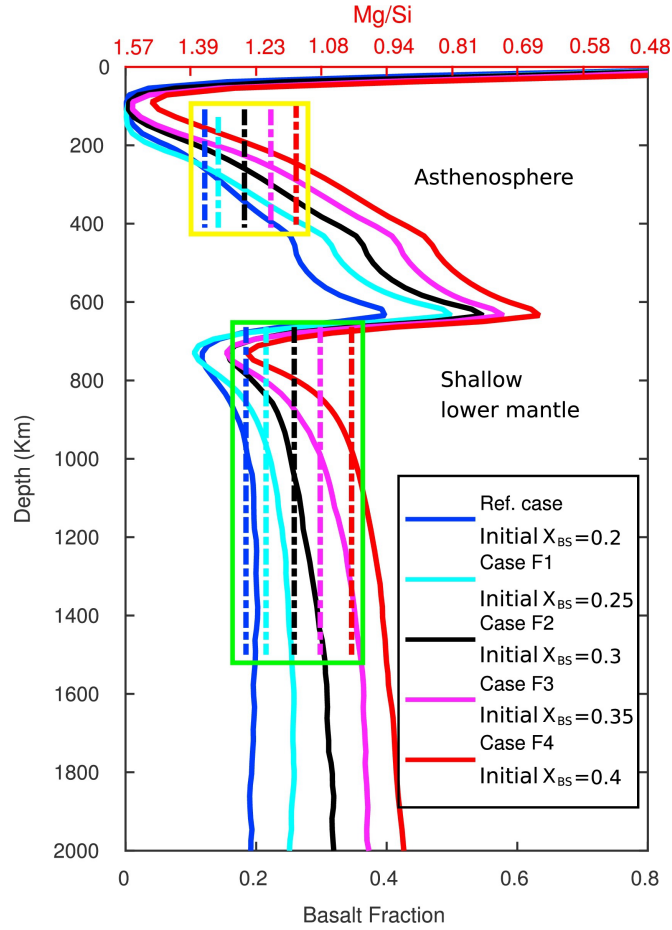


Fig. 8. Radial average X_{BS} (compositional index) between 2 and 4.5 Gyr for cases with different initial X_{BS} . Dashed lines in the yellow and green boxes denote average X_{BS} in the asthenosphere and shallow lower mantle, respectively.

4. Discussion

One of the most striking and robust predictions of our models is that subducted basalt and harzburgite segregate from each other near the CMB, and that basalt ultimately accumulates in

the MTZ and lower mantle. In turn, the asthenosphere and the layer just below 660 km depth are relatively depleted in basaltic components compared to the mantle average. These predictions result in systematic large-scale compositional layering on top of dominant small-scale and regional-scale variations, consistent with previous global-scale mantle-convection models that apply realistic density profiles for basalt and harzburgite (Ballmer et al., 2015; Nakagawa & Buffett, 2005; Nakagawa et al., 2010). Our results are controlled by the well-constrained density profiles of basalt and harzburgite (Fig. 1), and robust over a wide range of viscosity profiles (Fig. S3). Moderate mantle layering is predicted to be sustained by segregation despite ongoing whole-mantle convection and mixing, and to be soon established (within ~ 0.5 Gyr) after the onset of basalt cycling. This cycling could be due to plate tectonics, or another mechanism such as basalt dripping (Armann & Tackley, 2012), as likely relevant in the Archean (e.g., Fischer & Gerya, 2016, Johnson et al., 2014). In case mafic crust enters the mantle as a hybrid lithology such as pyroxenite (Bodinier & Godard, 2003; Castro & Gerya, 2008), the relevant density profile and hence the style of segregation and mixing are expected to differ from that modeled here.

As shown in section 3.4, this conclusion of moderate mantle layering implies that the composition of the bulk-silicate Earth (BSE) is shifted relative to upper(most)-mantle pyrolite. Indeed, such a difference in composition between the upper and lower mantles has been

proposed based on comparison of geophysical constraints with mineral-physics estimates of lower-mantle rock properties (e.g., [Murakami et al., 2012](#)). Moreover, recent sound-velocity measurements of CaSiO₃ perovskite ([Gréaux et al., 2019](#)) imply an enrichment of basaltic crust in the Earth's lower mantle.

An enhancement of the BSE in basaltic materials further implies an enrichment in SiO₂, as well as in Al₂O₃ and CaO, relative to pyrolite. Thus, our models can reconcile the high Mg/Si ratio of pyrolite with the compositional range of chondrites ([Ballmer et al., 2015](#)). Our models also imply superchondritic Earth Al/Si and Ca/Si (e.g., [McDonough & Sun, 1995](#)). Al/Si and Ca/Si would have to be less superchondritic for E-chondrite than the CI-chondrite Earth building blocks ([Javoy et al., 2010](#)), or if mafic materials stored in the lower mantle are largely ancient (e.g., Archean basalt, komatiite), and hence depleted in Al+Ca relative to modern MORB ([Hofmann & White, 1982](#); [Arndt et al., 2008](#)). In any case, our results point to some degree of fractionation of Al+Ca from Si+Mg during Earth accretion, which has been proposed to be due to a difference in condensation temperatures between Al+Ca and Si+Mg ([Hart & Zindler, 1986](#); [Lodders, 2003](#)).

In our models, the dynamic mechanisms for the transport of mantle materials to the MTZ are slabs, and most importantly, plumes. We find that the relevant processes, such as entrainment of basaltic materials by plumes in the deep mantle, failure of plumes to carry these materials across

the MTZ ([Nakagawa & Buffett, 2005](#)) and slab stagnation, depend on the mantle viscosity structure. Moreover, the prerequisite for any delivery of basaltic material to (and accumulation in) any mantle reservoir, i.e., the segregation of basalt from harzburgite, also depends on the viscosity structure of the mantle. Segregation is more efficient for larger scale-lengths of heterogeneity, and for lower viscosities ([Karato, 1997](#)), but should be efficient as long as mantle viscosity is sufficiently small in at least some regions of the mantle. Indeed, very low viscosities are locally promoted, e.g. in the hot thermal boundary layer, or post-perovskite stability field ([Ammann et al., 2010](#)). Despite these large effects of mantle rheology, our models predict the degree of enrichment of basalt in the MTZ to be rather robust (about $0.3 < X_{BS} < 0.35$) over a wide range of viscosity profiles (see also section 3.2), mostly due to a universal balance between delivery/removal and reservoir capacity. This is an encouraging result given that the radial mantle viscosity profile remains poorly constrained ([Rudolph et al., 2015](#)). Due to this control by MTZ capacity, we also do not expect that model simplifications (such as 2-D geometry) affect the final compositional profile significantly. Note that 2-D models artificially increase efficiency of basalt delivery to MTZ by implying sheet-like plumes, but they also display artificially poor segregation near the CMB ([Tackley, 2011](#)). Indeed, previous 3-D models predict compositional stratification across the MTZ (Figure 5 in [Nakagawa et al., 2010](#)), although high-resolution studies are needed for further quantitative investigation.

It has been suggested that some hotspots are sourced by plumes that originate from the MTZ (e.g., [Mazza et al., 2019](#)), while others are sourced by plumes that rise from the CMB, e.g. from the margins of thermochemical piles (e.g., [Burke et al., 2008](#)). However, it remains unclear how basalt can be transported from the MTZ reservoir to the surface. A possible explanation involves that sub-lithospheric small-scale convection ([Korenaga and Jordan, 2004](#)) entrains a certain amount of basalt from the MTZ reservoir. Alternatively, small-scale convection in, or hydrous upwellings from, the MTZ may be relevant for the segregation of basalt in the MTZ ([Long et al., 2019](#); [Motoki and Ballmer, 2015](#)). In our global-scale geodynamic models, such rather small-scale processes of convection and compositional segregation remain under-resolved due to computational limitations (low spatial resolution). Therefore, the compositional layering predicted here remains conservative.

Our robust model prediction of a basalt-reservoir in the MTZ, and a complementary harzburgite-reservoir just below, can be tested using seismic data. A long-standing discussion involves whether seismic properties of the MTZ can either be explained by a homogeneous pyrolite model ([Weidner, 1985](#)) or by a basalt-enriched model ([Agee, 1993](#)). An accumulation of harzburgite just below the MTZ can account for narrow high-velocity anomalies just beneath the MTZ in regions of mantle upwelling ([Maguire et al., 2017](#)). Based on a joint seismological and mineral-physics analysis, [Yu et al. \(2018\)](#) present direct evidence for local harzburgite enrichment near

the base of the MTZ beneath Hawaii. More recently, [Wu et al. \(2019\)](#) suggest chemical layering in regions with short-scale topography of the 660-km discontinuity. Note that our models also predict that a global reservoir can be maintained, at least for cases with relatively low reference viscosity, even though both slabs and plumes can destroy the formed basalt-enriched/harzburgite-enriched reservoir locally. However, more geophysical observations are needed to confirm the nature of regional, or even global, reservoirs near 660 km depth.

5. Conclusion

Our global-scale thermo-chemical convection models show that deep-rooted plumes (and to a minor extent, stagnant slabs) play an important role in terms of delivering basalt/harzburgite to the layers at the base/just below the MTZ, and to establish a laterally variable basalt-/harzburgite-enriched reservoir. The amount of basalt accumulated in the MTZ does not depend very much on the mantle viscosity structure, which is the result of a balance between delivery, removal and capacity of the MTZ. In turn, the amount of basalt accumulated above the CMB strongly depends on mantle viscosity structure. Our models predict that regional reservoirs in the MTZ are moderately-to-strongly enhanced by basalt (12%~37% on average) relative to pyrolite (i.e., compositional index 0.3~0.5), while most regional harzburgite-enriched reservoirs beneath the MTZ are enhanced by 40%~80% (compositional index 0.04~0.12). This prediction is

consistent with estimates from seismology, although more regional or even global studies are needed for further confirmation. The resulting compositional mantle layering is typically associated with a subadiabatic potential-temperature gradient across the MTZ. Finally, the composition of the bulk-silicate Earth may be shifted relative to that of the upper-mantle pyrolite if indeed significant reservoirs of basalt exist in the MTZ and lower mantle. Our results suggest that the segregation of basalt from harzburgite can act to filter mantle heterogeneity in order to sustain a layering mantle composition. The mantle flow that is related to sustaining the basalt-enriched MTZ (and harzburgite-enriched) reservoir may play an important role in regulating heat and material fluxes through the mantle.

Acknowledgments

We would like to thank the editor R. Bendick and two anonymous reviewers, whose comments and suggestions helped to improve the manuscript. P.T. acknowledges support from the Swiss Platform for Advanced Scientific Computing (StagBL project). Simulations were performed on the Euler and Leonhard clusters at ETH Zurich.

References

- Agee, C. B. (1993). Petrology of the mantle transition zone. *Annual Review of Earth and Planetary Sciences*, 21(1), 19-41.
- Allègre, C. J., & Turcotte, D. L. (1985). Geodynamic mixing in the mesosphere boundary layer and the origin of oceanic islands. *Geophysical Research Letters*, 12(4), 207-210.
- Ammann, M.W., Brodholt, J.P., Wookey, J., Dobson, D.P., 2010. First-principles constraints on diffusion in lower-mantle minerals and a weak D layer. *Nature* 465(7297), 462–465.
- Anderson, D. L. (1979). Chemical stratification of the mantle. *Journal of Geophysical Research: Solid Earth*, 84(B11), 6297-6298.
- Armann, M., & Tackley, P. J. (2012). Simulating the thermochemical magmatic and tectonic evolution of Venus's mantle and lithosphere: Two-dimensional models. *Journal of Geophysical Research: Planets*, 117(E12).
- Arndt, N.T., Leshar, C.M., & Barnes, S.J. (2008). *Komatiite*. Cambridge University Press, Cambridge. 467 pp.
- Ballmer, M. D., Houser, C., Hernlund, J. W., Wentzcovitch, R. M., & Hirose, K. (2017). Persistence of strong silica-enriched domains in the Earth's lower mantle. *Nature Geoscience*, 10(3), 236.

623 Ballmer, M. D., Schmerr, N. C., Nakagawa, T., & Ritsema, J. (2015). Compositional mantle
624 layering revealed by slab stagnation at ~1000-km depth. *Science advances*, 1(11), e1500815.

625 Ballmer, M. D., Schumacher, L., Lekic, V., Thomas, C. & Ito, G (2016). Compositional layering
626 within the large low shear-wave velocity provinces in the lower mantle. *Geochemistry,*
627 *Geophysics, Geosystems*, 17, 5056-5077.

628 Bentham, H. L. M., & Rost, S. (2014). Scattering beneath Western Pacific subduction zones:
629 evidence for oceanic crust in the mid-mantle. *Geophysical Journal International*, 197(3), 1627-
630 1641.

631 Bodinier, J. L., & Godard, M. (2003). Orogenic, ophiolitic, and abyssal peridotites. *Treatise on*
632 *geochemistry*, 2, 568.

633 Brandenburg, J. P., & Van Keken, P. E. (2007). Deep storage of oceanic crust in a vigorously
634 convecting mantle. *Journal of Geophysical Research: Solid Earth*, 112(B6).

635 Burke, K., Steinberger, B., Torsvik, T. H., & Smethurst, M. A. (2008). Plume generation zones
636 at the margins of large low shear velocity provinces on the core–mantle boundary. *Earth and*
637 *Planetary Science Letters*, 265(1-2), 49-60.

638 Castro, A., & Gerya, T. V. (2008). Magmatic implications of mantle wedge plumes:
639 experimental study. *Lithos*, 103(1-2), 138-148.

640 Christensen, U. R., & Hofmann, A. W. (1994). Segregation of subducted oceanic crust in the
641 convecting mantle. *Journal of Geophysical Research: Solid Earth*, 99(B10), 19867-19884.

642 Davies, G. F. (2008). Episodic layering of the early mantle by the 'basalt barrier'
643 mechanism. *Earth and Planetary Science Letters*, 275(3-4), 382-392.

644 Dziewonski, A. M., Lekic, V., & Romanowicz, B. A. (2010). Mantle anchor structure: an
645 argument for bottom up tectonics. *Earth and Planetary Science Letters*, 299(1-2), 69-79.

646 Fischer, R., & Gerya, T. (2016). Early Earth plume-lid tectonics: A high-resolution 3D numerical
647 modelling approach. *Journal of Geodynamics*, 100, 198-214.

648 Garnero, E. J., McNamara, A. K., & Shim, S. H. (2016). Continent-sized anomalous zones with
649 low seismic velocity at the base of Earth's mantle. *Nature Geoscience*, 9(7), 481.

650 Gréaux, S., Irifune, T., Higo, Y., Tange, Y., Arimoto, T., Liu, Z., & Yamada, A. (2019). Sound
651 velocity of CaSiO₃ perovskite suggests the presence of basaltic crust in the Earth's lower
652 mantle. *Nature*, 565(7738), 218.

653 Hart, S. R., & Zindler, A. (1986). In search of a bulk-Earth composition. *Chemical*
654 *Geology*, 57(3-4), 247-267.

655 Hirose, K., Fei, Y., Ma, Y., & Mao, H. K. (1999). The fate of subducted basaltic crust in the
656 Earth's lower mantle. *Nature*, 397(6714), 53.

657 Hofmann, A. W. (1997). Mantle geochemistry: the message from oceanic volcanism. *Nature*,
658 385(6613), 219.

659 Hofmann, A. W., & White, W. M. (1982). Mantle plumes from ancient oceanic crust. *Earth and*
660 *Planetary Science Letters*, 57(2), 421-436.

661 Irifune, T., & Ringwood, A. E. (1993). Phase transformations in subducted oceanic crust and
662 buoyancy relationships at depths of 600–800 km in the mantle. *Earth and Planetary Science*
663 *Letters*, 117(1-2), 101-110.

664 Ishii, M., & Tromp, J. (1999). Normal-mode and free-air gravity constraints on lateral variations
665 in velocity and density of Earth's mantle. *Science*, 285(5431), 1231-1236.

666 Javoy, M., Kaminski, E., Guyot, F., Andrault, D., Sanloup, C., Moreira, M., ... & Jaupart, C.
667 (2010). The chemical composition of the Earth: Enstatite chondrite models. *Earth and Planetary*
668 *Science Letters*, 293(3-4), 259-268.

669 Johnson, T. E., Brown, M., Kaus, B. J., & VanTongeren, J. A. (2014). Delamination and
670 recycling of Archaean crust caused by gravitational instabilities. *Nature Geoscience*, 7(1), 47.

671 Kaneshima, S., & Helffrich, G. (1999). Dipping low-velocity layer in the mid-lower mantle:
672 evidence for geochemical heterogeneity. *Science*, 283(5409), 1888-1892.

673 Karato, S. I. (1997). On the separation of crustal component from subducted oceanic lithosphere
674 near the 660 km discontinuity. *Physics of the Earth and Planetary Interiors*, 99(1-2), 103-111.

675 Koelemeijer, P., Ritsema, J., Deuss, A., & Van Heijst, H. J. (2015). SP12RTS: a degree-12
676 model of shear-and compressional-wave velocity for Earth's mantle. *Geophysical Journal*
677 *International*, 204(2), 1024-1039.

678 Korenaga, J., & Jordan, T. H. (2004). Physics of multiscale convection in Earth's mantle:
679 Evolution of sublithospheric convection. *Journal of Geophysical Research: Solid Earth*, 109(B1).

680 Lee, C. T. A., & Chen, W. P. (2007). Possible density segregation of subducted oceanic
681 lithosphere along a weak serpentinite layer and implications for compositional stratification of
682 the Earth's mantle. *Earth and Planetary Science Letters*, 255(3-4), 357-366.

683 Lodders, K. (2003). Solar system abundances and condensation temperatures of the
684 elements. *The Astrophysical Journal*, 591(2), 1220.

685 Long, X., Ballmer, M. D., Córdoba, A. M. C., & Li, C. F. (2019). Mantle melting and intraplate
686 volcanism due to self-buoyant hydrous upwellings from the stagnant slab that are conveyed by
687 small-scale convection. *Geochemistry, Geophysics, Geosystems*.

688 Maguire, R., Ritsema, J., & Goes, S. (2017). Signals of 660 km topography and harzburgite
689 enrichment in seismic images of whole-mantle upwellings. *Geophysical Research Letters*, 44(8),
690 3600-3607.

691 Mazza, S. E., Gazel, E., Bizimis, M., Moucha, R., Béguelin, P., Johnson, E. A., ... & Sobolev, A.
692 V. (2019). Sampling the volatile-rich transition zone beneath Bermuda. *Nature*, 569(7756), 398.

693 McDonough, W. F., & Sun, S. S. (1995). The composition of the Earth. *Chemical*
694 *geology*, 120(3-4), 223-253.

695 Motoki, M. H., & Ballmer, M. D. (2015). Intraplate volcanism due to convective instability of
696 stagnant slabs in the mantle transition zone. *Geochemistry, Geophysics, Geosystems*, 16(2), 538-
697 551.

698 Mukhopadhyay, S. (2012). Early differentiation and volatile accretion recorded in deep-mantle
699 neon and xenon. *Nature*, 486(7401), 101.

700 Mulyukova, E., Steinberger, B., Dabrowski, M., & Sobolev, S. V. (2015). Survival of LLSVPs
701 for billions of years in a vigorously convecting mantle: replenishment and destruction of
702 chemical anomaly. *Journal of Geophysical Research: Solid Earth*, 120(5), 3824-3847.

703 Mundl, A., Touboul, M., Jackson, M. G., Day, J. M., Kurz, M. D., Lekic, V., & Walker, R. J.
704 (2017). Tungsten-182 heterogeneity in modern ocean island basalts. *Science*, 356(6333), 66-69.

705 Murakami, M., Y. Ohishi, N. Hirao, and K. Hirose (2012), A perovskitic lower mantle inferred
706 from high-pressure, high-temperature sound velocity data, *Nature*, 485(7396), 90–U118.

707 Nakagawa, T., & Buffett, B. A. (2005). Mass transport mechanism between the upper and lower
708 mantle in numerical simulations of thermochemical mantle convection with multicomponent
709 phase changes. *Earth and Planetary Science Letters*, 230(1-2), 11-27.

710 Nakagawa, T., & Tackley, P. J. (2005). The interaction between the post-perovskite phase
711 change and a thermo-chemical boundary layer near the core–mantle boundary. *Earth and*
712 *Planetary Science Letters*, 238(1-2), 204-216.

713 Nakagawa, T., & Tackley, P. J. (2010). Influence of initial CMB temperature and other
714 parameters on the thermal evolution of Earth's core resulting from thermochemical spherical
715 mantle convection. *Geochemistry, Geophysics, Geosystems*, 11(6).

716 Nakagawa, T., & Tackley, P. J. (2012). Influence of magmatism on mantle cooling, surface heat
717 flow and Urey ratio. *Earth and Planetary Science Letters*, 329, 1-10.

718 Nakagawa, T., & Tackley, P. J. (2015). Influence of plate tectonic mode on the coupled
719 thermochemical evolution of Earth's mantle and core. *Geochemistry, Geophysics,*
720 *Geosystems*, 16(10), 3400-3413.

721 Nakagawa, T., Tackley, P. J., Deschamps, F., & Connolly, J. A. (2010). The influence of MORB
722 and harzburgite composition on thermo-chemical mantle convection in a 3-D spherical shell with
723 self-consistently calculated mineral physics. *Earth and Planetary Science Letters*, 296(3-4), 403-
724 412.

725 Ogawa, M. (2000). Numerical models of magmatism in convecting mantle with temperature-
726 dependent viscosity and their implications for Venus and Earth. *Journal of Geophysical*
727 *Research: Planets*, 105(E3), 6997-7012.

728 Ringwood, A. E. (1975). *Composition and Petrology of the Earth's Mantle*. McGraw-Hill, New
729 York.

730 Ringwood, A. E., & Irifune, T. (1988). Nature of the 650-km seismic discontinuity: implications
731 for mantle dynamics and differentiation. *Nature*, 331(6152), 131.

732 Rizo, H., Boyet, M., Blichert-Toft, J., & Rosing, M. T. (2013). Early mantle dynamics inferred
733 from ^{142}Nd variations in Archean rocks from southwest Greenland. *Earth and Planetary Science*
734 *Letters*, 377, 324-335.

735 Rost, S., Garnero, E. J., & Williams, Q. (2008). Seismic array detection of subducted oceanic
736 crust in the lower mantle. *Journal of Geophysical Research: Solid Earth*, 113(B6).

737 Rudolph, M. L., Lekić, V., & Lithgow-Bertelloni, C. (2015). Viscosity jump in Earth's mid-
738 mantle. *Science*, 350(6266), 1349-1352.

739 Sinha, G., & Butler, S. L. (2007). On the origin and significance of subadiabatic temperature
740 gradients in the mantle. *Journal of Geophysical Research: Solid Earth*, 112(B10).

741 Stixrude, L., & Lithgow-Bertelloni, C. (2012). Geophysics of chemical heterogeneity in the
742 mantle. *Annual Review of Earth and Planetary Sciences*, 40, 569-595.

743 Tackley, P. J. (2008). Modelling compressible mantle convection with large viscosity contrasts
744 in a three-dimensional spherical shell using the yin-yang grid. *Physics of the Earth and Planetary*
745 *Interiors*, 171(1-4), 7-18.

746 Tackley, P. J. (2011). Living dead slabs in 3-D: The dynamics of compositionally-stratified slabs
747 entering a "slab graveyard" above the core-mantle boundary. *Physics of the Earth and Planetary*
748 *Interiors*, 188(3-4), 150-162.

749 Tackley, P. J. (2012). Dynamics and evolution of the deep mantle resulting from thermal,
750 chemical, phase and melting effects. *Earth-Science Reviews*, 110(1-4), 1-25.

751 van Keken, P. E., Karato, S., & Yuen, D. A. (1996). Rheological control of oceanic crust
752 separation in the transition zone. *Geophysical Research Letters*, 23(14), 1821-1824.

753 Waszek, L., Schmerr, N. C., & Ballmer, M. D. (2018). Global observations of reflectors in the
754 mid-mantle with implications for mantle structure and dynamics. *Nature communications*, 9(1),
755 385.

756 Weidner, D. J. (1985). A mineral physics test of a pyrolite mantle. *Geophysical Research Letters*,
757 12(7), 417-420.

758 Wu, W., Ni, S., & Irving, J. C. (2019). Inferring Earth's discontinuous chemical layering from
759 the 660-kilometer boundary topography. *Science*, 363(6428), 736-740.

760 Xu, W., Lithgow-Bertelloni, C., Stixrude, L., & Ritsema, J. (2008). The effect of bulk
761 composition and temperature on mantle seismic structure. *Earth and Planetary Science Letters*,
762 275(1-2), 70-79.

763 Yu, C., Day, E. A., Maarten, V., Campillo, M., Goes, S., Blythe, R. A., & van der Hilst, R. D.
764 (2018). Compositional heterogeneity near the base of the mantle transition zone beneath Hawaii.
765 *Nature communications*, 9(1), 1266.